Dynamics of an oscillating turbulent jet in a confined cavity

Righolt, BW; Kenjeres, S; Kalter, R; Tummers, MJ; Kleijn, CR

DOI
10.1063/1.4930926

Publication date
2015

Document Version
Final published version

Published in
Physics of Fluids

Dynamics of an oscillating turbulent jet in a confined cavity

B. W. Righolt, S. Kenjereš, R. Kalter, M. J. Tummers, and C. R. Kleijn

Citation: Physics of Fluids **27**, 095107 (2015); doi: 10.1063/1.4930926
View online: http://dx.doi.org/10.1063/1.4930926
View Table of Contents: http://scitation.aip.org/content/aip/journal/pof2/27/9?ver=pdfcov
Published by the AIP Publishing

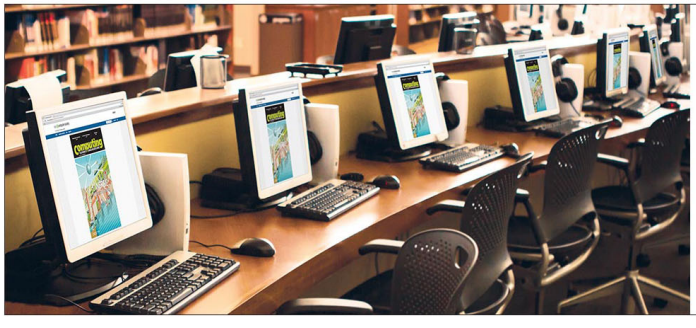

Dynamics of an oscillating turbulent jet in a confined cavity

B. W. Righolt,[1,2,a)] S. Kenjereš,[1,2] R. Kalter,[1,2] M. J. Tummers,[2,3] and C. R. Kleijn[1,2]

[1]*Department of Chemical Engineering, Faculty of Applied Sciences, Delft University of Technology, Julianalaan 136, 2628 BL Delft, The Netherlands*
[2]*J.M. Burgerscentre for Fluid Mechanics, Delft, The Netherlands*
[3]*Laboratory for Aero and Hydrodynamics, Delft University of Technology, Leeghwaterstraat 21, 2628 CA Delft, The Netherlands*

(Received 23 November 2014; accepted 1 September 2015; published online 17 September 2015)

We demonstrate how the self-sustained oscillation of a confined jet in a thin cavity can be quantitatively described by a zero-dimensional model of the delay differential equation type with two *a priori* predicted model constants. This model describes the three phases in self-sustained oscillations: (i) pressure driven growth of the oscillation, (ii) amplitude limitation by geometry, and (iii) delayed destruction of the recirculation zone. The two parameters of the model are the growth rate of the jet angle by a pressure imbalance and the delay time for the destruction of this pressure imbalance. We present closed relations for both model constants as a function of the jet Reynolds number Re, the inlet velocity v_{in}, the cavity width W, and the cavity width over inlet diameter W/d and we demonstrate that these model constants do not depend on other geometric ratios. The model and the obtained model constants have been successfully validated against three dimensional large eddy simulations, and planar particle image velocimetry measurements, for $1600 < Re \leq 7100$ and $20 \leq W/d < 50$. The presented model inherently contains the transition to a non-oscillating mode for decreasing Reynolds numbers or increasing W/d-ratios and allows for the quantitative prediction of the corresponding critical Reynolds number and critical W/d. © *2015 AIP Publishing LLC.* [http://dx.doi.org/10.1063/1.4930926]

I. INTRODUCTION

A fluid jet may demonstrate self-sustained oscillations when it is confined in both directions perpendicular to its flow direction. This phenomenon has been observed for jet Reynolds numbers ranging from $Re = 100$[1–4] up to $Re = 170\,000$.[5] The physical mechanism for this oscillation is well understood for both laminar[2] and turbulent[6] jets. The dimensions of the confining cavity are known to have an important influence on the presence and frequencies of these oscillations. For very wide cavities, the domain becomes unbounded in one direction, and the self-sustained oscillation disappears.[7] A jet in such a wide cavity shows meandering, self-similar behavior.[8] For decreasing cavity width, the oscillation frequency increases,[7,9] until the cavity geometry approaches that of a sudden expansion, where strong asymmetries and oscillations are present as well.[10–12] A vast amount of fluidic oscillators exists,[3,6,13,14] which are, for example, found in backward facing steps, flows over cavities,[15] and jets through orifices.[16] The systems have in common that either implicitly or explicitly a delayed feedback loop is present that triggers the oscillatory behavior.

Delayed feedback mechanisms are very common in nature and technology and can result in oscillations of any type. Some of these mechanisms can be described by a delay differential equation (DDE) with a single delay constant. The delay time between the uptake of oxygen in the lungs and the reception in the brain stem plays a role in the arterial CO_2 control system.[17] In economics,

a)Electronic mail: b.w.righolt@tudelft.nl

the interplay between income and capital stock can be explained with a time delay in investments.[18] Another example is the large time scale temperature oscillation on the southern hemisphere, often referred to as *El Niño*, with a delay time that is associated with the transit time of Rossby and Kelvin waves across the Pacific ocean.[19,20] DDE models have also been proposed for the oscillation of the reattachment length in a confined jet flow[2] or for convective rolls in a closed box.[21] Although the physical mechanism active in each of the above examples may be very different, they have all been successfully described with DDE-type models.

The objective of the present study is (i) to develop a DDE-type model for the oscillations of a turbulent jet in a confined cavity, which represents the physical phases of the oscillating motion and (ii) to use this model to predict necessary conditions for the existence of self-sustained oscillations depending on the jet Reynolds number Re, and cavity width to nozzle diameter ratio W/d. We use both large eddy simulations (LES) and experimental data to validate our DDE model and its predictions.

The paper is outlined as follows. The confined jet configuration and numerical methods for 3D LES turbulent flow simulations are given in Section II, the experimental validation of the numerical flow simulations is presented in Section III. In Section IV, we present a zero-dimensional DDE-type model for single jet oscillations in a confined cavity and in Section V we discuss how the model parameters in the DDE model can be obtained from given flow properties.

II. METHODS

A. Description of setup

In this paper, we study the flow in a cavity as depicted in Figure 1. This cavity has dimensions height × width × thickness ($H \times W \times T$). A downward oriented square tube of inner dimensions d is inserted centrally to a depth d_n, which injects the fluid into the cavity with a velocity v_{in}. For $H \times W \times T = 0.7 \times 0.3 \times 0.035$ m^3, $d = 0.01$ m, and $d_n = 0.1$ m, the flow of salt water in this configuration is essentially two-dimensional, as will be demonstrated further in this paper by showing its insensitivity to the precise value of T, and to friction at the front and back walls. The flow in this configuration was previously investigated experimentally using planar particle imaging velocimetry by Kalter *et al.*[6] The outflow was placed off center, in order to allow for optical access. In the present study, we use the same dimensions H, T, d, d_n, whereas the width W is varied between $W/d = 10$ and $W/d = 100$. For the cases $W/d \geq 50$, the height H was increased to $H/W = 2.5$. The top of the cavity is a free surface and the working fluid has a density $\rho = 1.1 \times 10^3$ kg m^{-3} and viscosity $\nu = 1.27 \times 10^{-6}$ m^2 s^{-1}.

In Figure 1, the instantaneous jet angle θ is defined. The jet angle was determined by a least squares fit of a straight line through the points $x_i = \max_x(|v(y_i)|)$, in other words, through the x-coordinates of the locations of maximum velocity magnitude for every line $y = y_i$ in the range $(-d_n - S) < y_i < (-d_n)$, where we set S equal to W. Figure 2 shows the collections (x_i, y_i) and the resulting linear fit for three time instances in half a period of the oscillation.

B. Numerical fluid flow models

We consider the LES filtered, single phase, incompressible Navier-Stokes equations,

$$\frac{\partial v_i}{\partial t} + v_j \frac{\partial v_i}{\partial x_j} = \frac{\partial}{\partial x_j}\left[(\nu + \nu_{SGS})\left(\frac{\partial v_i}{\partial x_j} + \frac{\partial v_j}{\partial x_i}\right)\right] - \frac{1}{\rho}\frac{\partial p}{\partial x_i}, \tag{1}$$

where v_i is the velocity, ρ the fluid density, ν the laminar viscosity, ν_{SGS} the sub-grid-scale viscosity from the LES model, and p the pressure. We use the finite-volume based tool OpenFOAM 2.1[22] to solve the discretized equations using the PISO scheme.[23]

The dynamic Smagorinsky model[24] has been employed to calculate the sub-grid-scale viscosity as $\nu_{SGS} = (C\Delta)^2\mathcal{S}$, where Δ is the local grid size, defined as $\Delta = \left(\Delta_x\Delta_y\Delta_z\right)^{1/3}$ and $\mathcal{S}$ the characteristic rate of strain, $\mathcal{S} = \left(2S_{ij}S_{ij}\right)^{1/2}$ and $S_{ij} = \left(\partial v_i/\partial x_j + \partial v_j/\partial x_i\right)/2$. The Smagorinsky

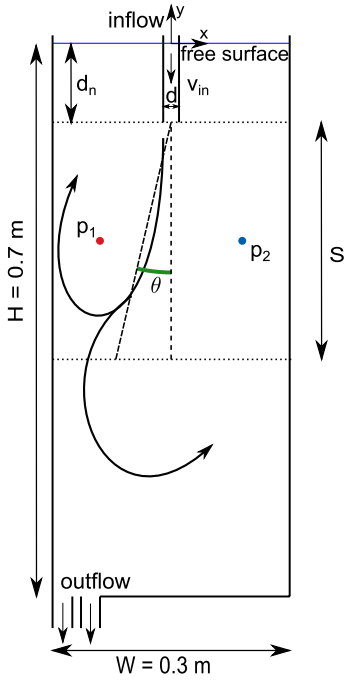

FIG. 1. Studied configuration of a single jet in a confined geometry. The cavity has dimensions $H \times W \times T = 0.7 \times 0.3 \times 0.035$ m^3. The nozzle inner width is $d = 0.01$ m and is submerged by a distance $d_n = 0.1$ m. The definition of the instantaneous jet angle θ, which is calculated between the nozzle exit and a line at a distance S downstream from the nozzle exit, and monitoring locations p_1 and p_2 are indicated.

constant C is defined as $C = \langle L_{ij} M_{ij} \rangle / 2 \left\langle M_{ij}^2 \right\rangle$, with the resolved stress tensor $L_{ij} = \widetilde{v_i v_j} - \tilde{v}_i \tilde{v}_j$ and $M_{ij} = 2\Delta^2 \widetilde{\mathcal{S}\mathcal{S}_{ij}} - 2(2\Delta)^2 \tilde{\mathcal{S}} \tilde{\mathcal{S}}_{ij}$, where $\tilde{\cdot}$ indicates the filtering operation. An important advantage of the dynamic Smagorinsky model for the studied application is that it automatically handles the damping of turbulence towards the walls.

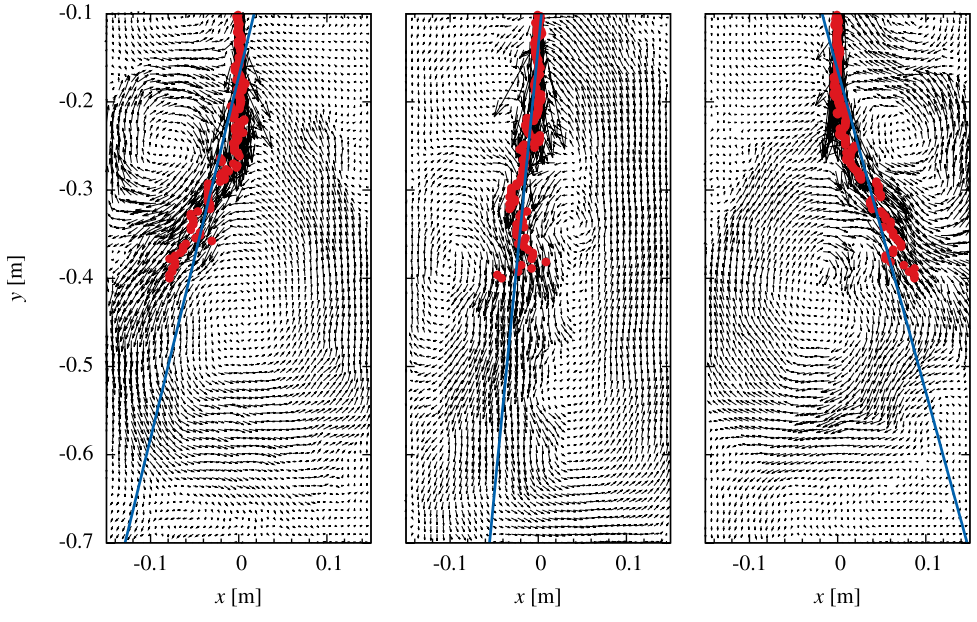

FIG. 2. The instantaneous jet angle is calculated from a least squares fit (blue line) through the points of maximum velocity (red dots) per y-coordinate in the instantaneous velocity field obtained from the numerical simulation (black vectors). Here shown for $Re = 4700$ and $W/d = 30$ at $t = 64$ s (left), a quarter period later at $t = 74$ s and half a period later at $t = 84$ s.

As recommended by Lilly,[24] we use local averaging (indicated by $\langle . \rangle$) of the Smagorinsky coefficient in order to reduce computational instabilities, due to local small values of M_{ij}^2. We follow the approach of Zang, Street, and Koseff[25] and apply averaging over three control volumes in every direction, as well as clipping of the total viscosity $\nu + \nu_{SGS}$ at 0, in order to partially allow for backscatter, i.e., the transfer of energy to larger scales.[24] For the studied applications, the region where $\nu_{SGS}/\nu < -0.5$ occupies less than 1% of the total domain.

The equations are discretized on an orthogonal, rectangular mesh, consisting of $128 \times 275 \times 34 \approx 1.1 \times 10^6$ grid cells. This being a sufficient grid resolution is demonstrated in Figure 3 (bottom), which shows contours of the instantaneous ν_{SGS}/ν. The maximum value $\nu_{SGS}/\nu \leq 10$, and the domain averaged $\nu_{SGS}/\nu = 0.1$.

Temporal discretization is done using a second order fully implicit scheme,[22] with a time step corresponding to $\max(Co = u\Delta t/\Delta x) = 1$. Within the distributed version of OpenFoam, higher order explicit temporal discretization schemes are not available. Moreover, Vuorinen *et al.* have shown that their implementation and application of a third and fourth Runge-Kutta explicit temporal discretization within OpenFOAM led to a small efficiency gain only.[26] The convective and diffusive terms are spatially discretized using a second order central differencing scheme.

The instantaneous value of y^+ at the walls locally reaches values as low as $y^+ = 0.1$ and as high as $y^+ = 15$. We therefore apply, at all solid wall boundaries, a universal velocity profile called Spalding's law,[27] viz., $y^+ = u^+ + 1/E\left[\exp(\kappa u^+) - \left(1 + \kappa u^+ + 1/2(\kappa u^+)^2 + 1/6(\kappa u^+)^3\right)\right]$, with $y^+ = y u_\tau/\nu$, $u^+ = v/u_\tau$, the friction velocity $u_\tau^2 = (\nu + \nu_{SGS})\, dv/dn$, $\kappa = 0.41$, and $E = 9.8$.[28–31] This law is valid for $0 \leq y^+ \leq 300$ and we therefore generally apply it to all walls of the domain. For $y^+ < 10$, which is the case for most parts of the walls, Spalding's law reduces to the laminar flow no-slip boundary condition. Indeed, using a laminar flow boundary condition instead of Spalding's law led to minor changes in the flow behaviour only. This also indicates that our simulations are relatively insensitive to the near-wall grid size.

For the inflow via the nozzle, a periodic inlet domain, of length $10d$, was applied to guarantee fully developed inflow conditions. The free liquid surface at $y = 0$ was modeled using a free slip boundary condition.

III. VALIDATION OF THE NUMERICAL METHOD

We validate the numerical model for a jet of $Re = v_{in} d/\nu = 4700$ in a confined cavity as defined in Figure 1 using data from our previous experiments.[6] In Figure 3, vectors of the mean velocity and contours of the horizontal and vertical components of the mean velocity are depicted, both for the present numerical simulation and for the experiment. In Figure 4, the vertical component of the mean velocity on three horizontal lines downstream from the nozzle is depicted. These comparisons show a good agreement between numerical and experimental mean velocities.

Figure 4 furthermore shows profiles of the turbulent kinetic energy obtained from the numerical simulations, where at each distance a double peak is observed, which is related to the long term oscillations of the jet in the cavity.

Figure 5 shows a time series of the jet angle for both the numerical simulations and the experiments. The dominant frequency of oscillation was determined at $f = 0.022 \pm 0.001$ Hz for the simulations and $f = 0.023 \pm 0.002$ Hz for the experiments. This leads to a Strouhal number $St = fW/v_{in}$ of $St = 0.011$, which is in accordance with findings from the literature.[6]

IV. MODEL FOR SELF-SUSTAINED OSCILLATIONS OF A JET IN A CONFINED CAVITY

A. Physical mechanisms

The physical mechanism of the stable self-sustained oscillation of a single jet in a closed, thin cavity has been described earlier to consist of three stages.[6] Initially, the jet flows straight to the bottom, forming two recirculation zones of equal size on both sides of the cavity. Then, due to a small, random pressure difference across the jet, it will move towards one side of the cavity (designated right in this section), after which the self-sustained oscillation is triggered.

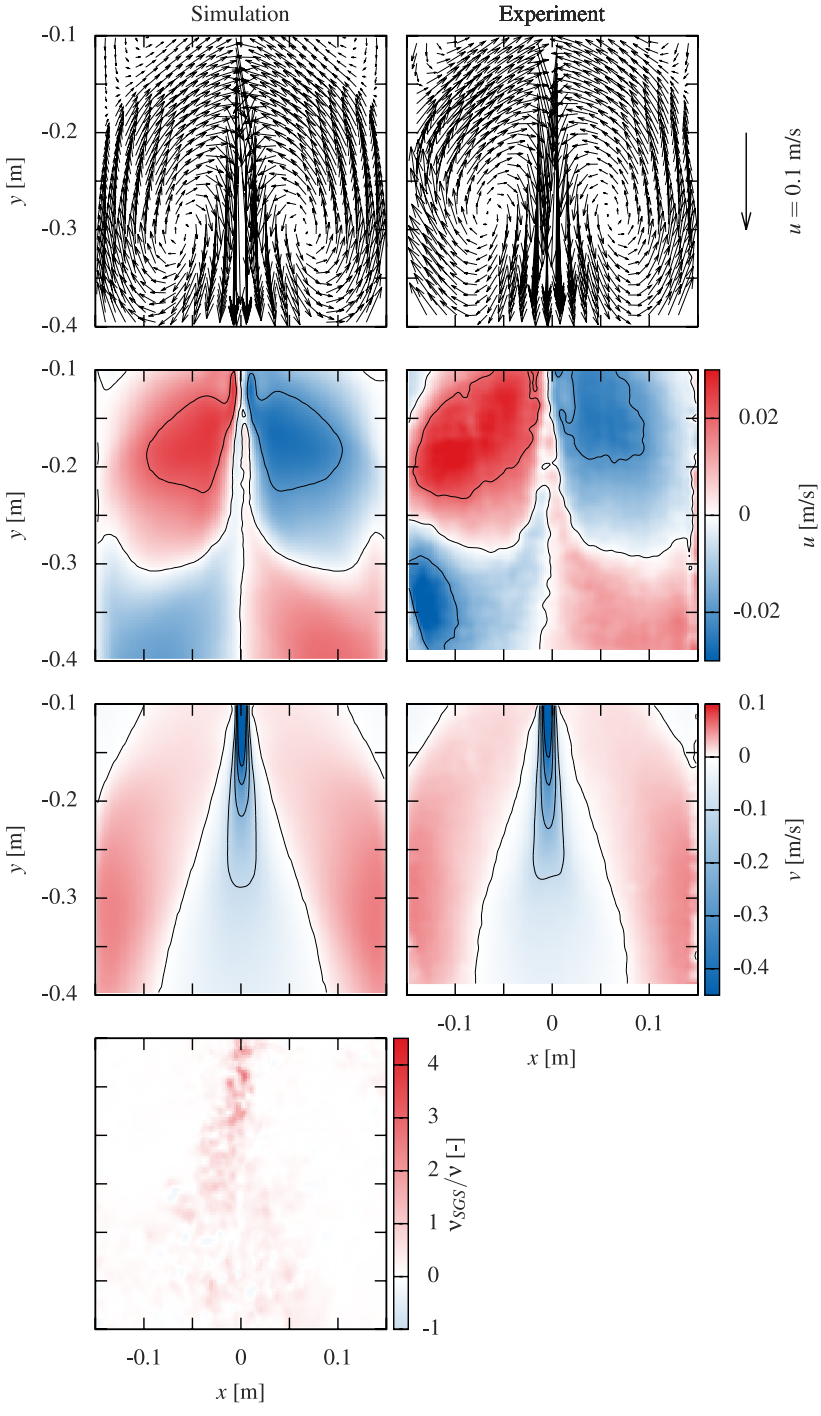

FIG. 3. For $Re = 4700$ and $W/d = 30$ in the $z = 0$-plane, simulation (left) and experiment (right), from top to bottom: vector fields of the mean velocity, contours of the horizontal mean velocity, contours of the vertical mean velocity, and contours of the scaled instantaneous sub-grid-scale viscosity ν_{SGS}/ν.

In the first stage of the jet oscillation, the jet is oriented slightly to the right ($\theta < 0$), which causes the recirculation zone at the right to be slightly stronger, due to its smaller diameter and higher velocities. This causes a larger pressure deficit in this recirculation zone, which draws the jet further towards the side, hence again creating a larger pressure deficit and further jet deflection.

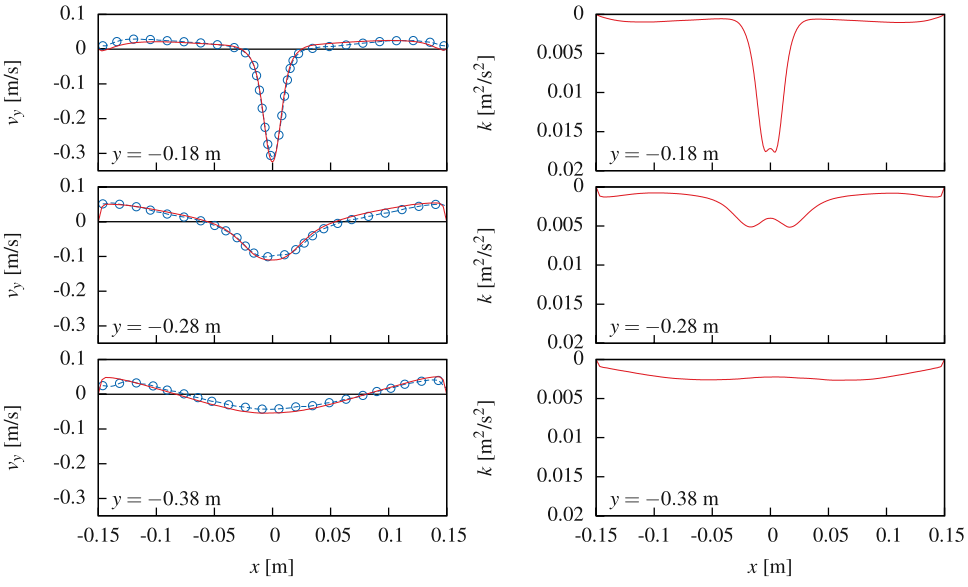

FIG. 4. (Left) The vertical component of the mean velocity for $Re = 4700$ and $W/d = 30$ for the lines $y = -0.18$ m, $y = -0.28$ m, and $y = -0.38$ m, which is, respectively, 0.08 m, 0.18 m, and 0.28 m below the nozzle exit for both the numerical simulation (solid red) and the experiments (dashed blue and circles, Kalter *et al.*[6]). (Right) The turbulent kinetic energy obtained from the numerical simulations is shown for the same lines (red).

Thus, the jet angle and pressure deficit in the recirculation zone are tightly coupled. We confirm this by means of our LES simulations. The time dependency of both the jet angle θ and the pressure difference Δp across the jet, obtained from these simulations, is shown in Figure 6 (left) for $Re = 4700$, where Δp was determined from the pressure difference, $\Delta p = p_2 - p_1$, between the monitoring points p_1 and p_2, as defined in Figure 1 and θ is defined to be positive for jet deflections to the left.

It is seen from Figure 6 (left) that θ and Δp oscillate with the same period $\mathcal{T} = 46$ s. The pressure signal is slightly ahead of the jet angle signal, especially during the sweeping motion of the jet far from its extreme positions. The cross correlation function (see Figure 6 (right)) of both signals shows a peak around $\Delta t = 2$ s, which means that the jet angle follows the pressure difference with a small time delay of 2 s. At the extreme positions, other effects take over, and the phase difference is not clearly visible anymore. These observations and the found time delay were found to be rather insensitive to the choice of the location of probe-points p_1 and p_2.

Next, in the second stage of the jet oscillation, the jet approaches the side wall and the recirculation zone cannot shrink any further, because this would lead to a strongly non-circular recirculation zone with relatively high velocities, which becomes unphysical. At that moment, the maximum

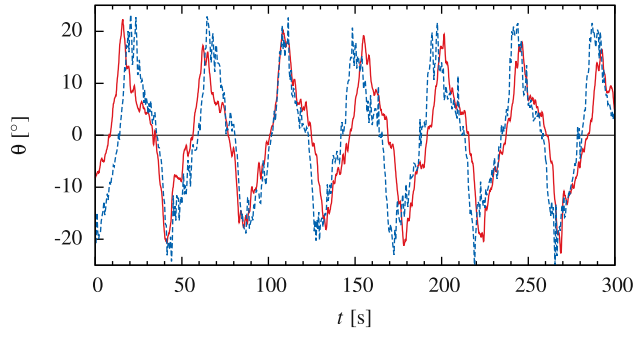

FIG. 5. Jet angle $\theta(t)$ from the numerical simulation (solid red line) and from the PIV measurements (dashed blue line, from Kalter *et al.*[6]) for $Re = 4700$ and $W/d = 30$.

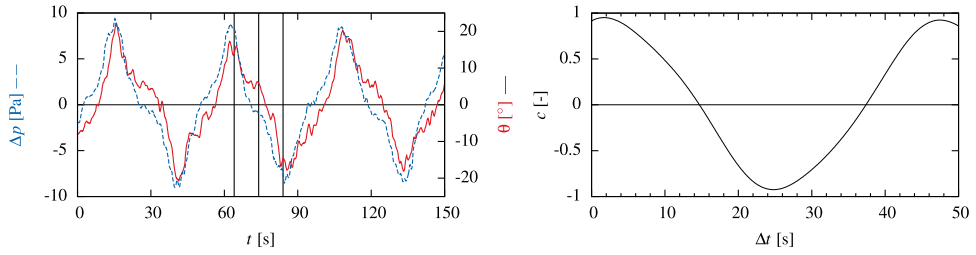

FIG. 6. (Left) Time series of the pressure difference between monitoring point p_1 and p_2 (as defined in Figure 1) (dashed blue) and a time series of the jet angle θ (solid red) for $Re = 4700$. The vertical lines indicate the time instances for the snap shots in Figure 2. (Right) Cross correlation function between Δp and θ.

jet deflection θ_{max} is reached. Now, the driving mechanism in the increasing pressure deficit in the upper recirculation zone vanishes, and the driving motion for the jet deflection therefore also vanishes.

With reference to Figure 2 (right) we can estimate θ_{max}. In the extreme right position of the jet ($\theta = -\theta_{max}$), a recirculation zone of diameter $W/2$ is present in the upper right corner, and a second adjacent recirculation zone of diameter W lower in the cavity. Now, for the angle θ between the vertical and the line connecting the nozzle exit with the tangent point of the two recirculation zones, we find from simple geometrical considerations[32] $\tan(\theta) = \left(\frac{3}{2} + \sqrt{2}\right)^{-1}$, or $\theta \approx 19°$.

Indeed, in our simulations, we find a constant $\theta_{max} = 18°$ independent of Re for a wide range of W/d. In Figure 7, both a time series and a phase averaged jet angle are shown for Reynolds numbers between $Re = 3150$ and $Re = 7100$. The jet angle amplitude is almost independent of Re. The oscillation frequency, however, differs significantly, with periods increasing roughly inversely proportional with Re, from $\mathcal{T} = 31$ s to $\mathcal{T} = 59$ s upon decreasing Re from 7100 to 3150. This is in accordance with the constant Strouhal number behavior as determined by Kalter *et al.*[6] In Figure 8, W/d is varied between 10 and 50. The frequency of oscillation increases with decreasing W/d, in correspondence with findings of Lawson and Davidson.[9] It should be noted that $W/d = 10$ is the geometry ratio previously studied by Villermaux and Hopfinger.[2] The amplitude θ_{max} of the oscillation is only weakly dependent on W/d for $W/d \geq 20$.

Finally, the third and final stage starts when the jet oscillation has reached its maximum deflection angle and the jet impinges on the side wall. This causes a division of flow between an upper, strong recirculation zone and a downward directed flow along the wall. The downward flow along the right wall starts to feed a recirculation zone in the lower left part of the cavity. This new recirculation zone is visible in Figure 2 (right). The diminishing flow rate in the upper recirculation zone results in a smaller pressure deficit in the centre of the upper recirculation zone. Simultaneously, the secondary recirculation zone lower in the cavity starts to grow in strength. Less fluid is fed to the recirculation zone in the upper right part of the cavity, which causes the pressure deficit inside the upper right recirculation zone to quickly decrease. The jet will not remain in its extreme position, $-\theta_{max}$, but will move downward and subsequently towards the left, with θ returning to 0,

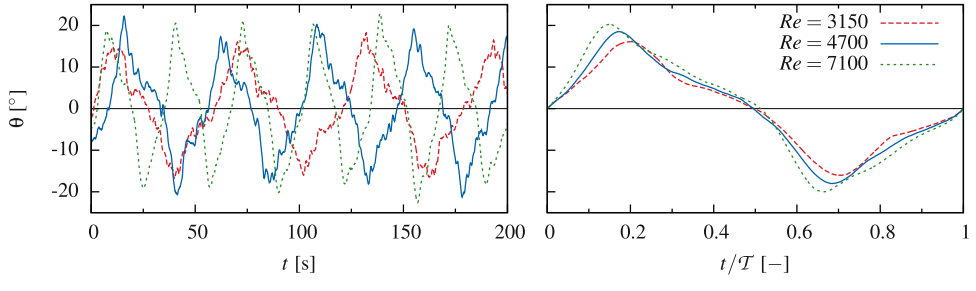

FIG. 7. (Left) Time series of the jet angle θ and (right) phase average jet angle profile normalized by the period $\mathcal{T}$, for $Re = 3150$ (dashed red), $Re = 4700$ (solid blue), and $Re = 7100$ (long-dashed green) with period $\mathcal{T} = 59$ s, $\mathcal{T} = 46$ s, and $\mathcal{T} = 31$ s, respectively.

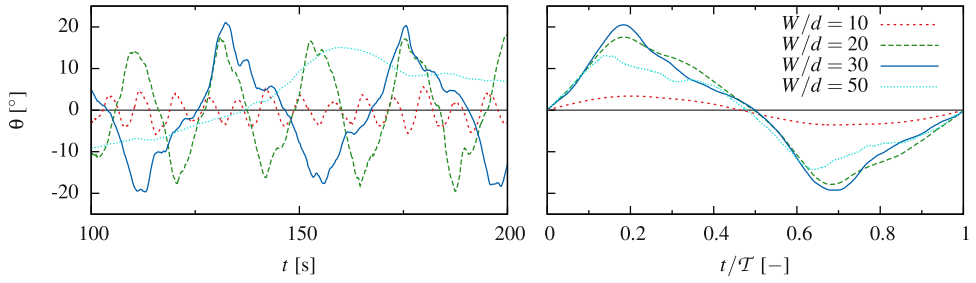

FIG. 8. (Left) Time series of the jet angle $\theta(t)$ and (right) phase average jet angle profile, with the time-axis scaled by the period $\mathcal{T}$, for $Re = 4700$ and $W/d = 10$ (dashed red), $W/d = 20$ (long-dashed green), $W/d = 30$ (solid blue), and $W/d = 50$ (short-dashed turquoise), and $\mathcal{T} = 7.5$ s, $\mathcal{T} = 22$ s, $\mathcal{T} = 43$ s, and $\mathcal{T} = 1.8 \times 10^2$ s, respectively.

as follows from Figure 6. The decay of the strong recirculation zone is associated with a delay time scale τ, which plays a crucial role in the self-sustained nature of the oscillation. As the jet crosses the vertical at $\theta = 0$, the first stage re-starts. This self-sustained oscillation repeats itself indefinitely.

B. Model description

In this section, we propose a zero-dimensional model for the self-sustained jet oscillation in a confined cavity based on the relevant physical mechanisms. We start from the horizontal component of the Navier-Stokes equations,

$$\frac{\partial v_x}{\partial t} + v_x \frac{\partial v_x}{\partial x} + v_y \frac{\partial v_x}{\partial y} = -\frac{1}{\rho}\frac{\partial p}{\partial x} + \nu \frac{\partial^2 u_x}{\partial x^2} + \nu \frac{\partial^2 u_x}{\partial y^2}. \tag{2}$$

Neglecting the viscous terms in this equation due to the high Reynolds number of the flow, we show that on the left hand side of this equation, the third term is dominant. First, v_x is estimated from the jet oscillation, i.e., $v_x \sim -S\frac{\partial \theta}{\partial t} \sim -\frac{S\theta_{max}}{\mathcal{T}}$, and v_y is estimated from $v_y \sim v_{in}$. An order of magnitude analysis leads to

$$\frac{\frac{\partial v_x}{\partial t}}{v_y \frac{\partial v_x}{\partial y}} \sim \frac{\frac{S\theta_{max}}{\mathcal{T}^2}}{v_{in}\frac{S\theta_{max}}{\mathcal{T}S}} \sim \frac{S}{v_{in}\mathcal{T}}, \qquad \frac{v_x \frac{\partial v_x}{\partial x}}{v_y \frac{\partial v_x}{\partial y}} \sim \frac{\frac{S^2\theta_{max}^2}{\mathcal{T}^2 W}}{v_{in}\frac{S\theta_{max}}{\mathcal{T}S}} \sim \frac{S^2\theta_{max}}{v_{in}\mathcal{T}W}. \tag{3}$$

Observing from Figure 2 that $S \sim W$ and using the observation that $St = W/(v_{in}\mathcal{T}) \ll 1$, we now find that

$$\frac{\frac{\partial v_x}{\partial t}}{v_y \frac{\partial v_x}{\partial y}} \sim St \ll 1, \qquad \frac{v_x \frac{\partial v_x}{\partial x}}{v_y \frac{\partial v_x}{\partial y}} \sim St\,\theta_{max} \ll 1. \tag{4}$$

From Equation (2), two leading terms remain,

$$v_y \frac{\partial v_x}{\partial y} \sim -\frac{1}{\rho}\frac{dp}{dx}, \tag{5}$$

which can be rewritten using the above expressions for v_x and v_y, and recalling $\Delta p = p_2 - p_1$, to

$$\frac{d\theta}{dt} \propto \frac{1}{\rho v_{in} W}\Delta p. \tag{6}$$

From Figure 6, we observed that θ and Δp are tightly coupled. Hence, we may pose

$$\Delta p \propto \theta. \tag{7}$$

Now, combining Equations (6) and (7), we find that, during the growing stage of the jet oscillation,

$$\frac{d\theta}{dt} = r\theta, \tag{8}$$

where r is the growth rate of the jet oscillation. This expression is not a sufficient description for the time evolution of the jet behaviour, as it does not incorporate the maximum achievable jet angle and consecutive decay of the upper recirculation zone.

The maximum achievable jet angle acts as a damping mechanism on the self-excited jet oscillation, as it prevents unlimited growth of the jet angle. Hence, we introduce an obstruction parameter, μ, and introduce a damping term in Equation (8),

$$\frac{d}{dt}\theta = (r - \mu\theta^2)\theta. \tag{9}$$

The third order of the damping term in θ is chosen as the lowest possible order which is (i) higher than the order of the leading forcing term and (ii) able to maintain symmetry of the model equation. The equation now has three equilibrium points, namely, $\theta = 0$, which is unstable, and $\theta = \pm\sqrt{r/\mu}$, which are stable equilibria. Thus, the value of the obstruction parameter μ is related to the growth rate parameter r and to the maximum deflection angle θ_{max} as $\mu = r/\theta_{max}^2$. Later, we show that the inclusion of the feedback term in the model, as discussed below, leads to a small correction in μ.

As described above, the delay time τ is associated with the decay time of the strong recirculation zone, eventually restoring the jet angle θ. This is represented in model Equation (10) by the negative feedback term, with a feedback strength k, and $k < r$. The delay time τ is of the order of the turnover time of the recirculation zone, which scales with W/v_{in}. Later, we will show that it is also weakly dependent on Re.

This leads to the full model equation

$$\frac{d}{dt}\theta(t) = r\theta(t) - \mu\theta^3(t) - k\theta(t-\tau), \tag{10}$$

where r, μ, k, and τ are the model parameters described above. This is an example of a retarded delay differential equation[33] and is also referred to as delayed-action oscillator. In this form, it is used, for example, in the description of the El Niño oscillation.[19,20] The three terms on the right hand side of the equation can be associated with the three stages in the oscillating motion as described above.

V. DETERMINATION OF MODEL PARAMETERS AND ITS IMPLICATIONS

We now discuss how the four model parameters r, μ, k, and τ in Equation (10) can be predicted *a priori*, as a function of Re and W/d. From LES simulations at given W/d and Re, we computationally determine the best fitting parameter set $\{r, \mu, k, \tau\}$, by applying the Nelder-Mead simplex method[34] on the phase-averaged jet angle. This procedure is further outlined in the Appendix.

Figure 9 shows the phase-averaged jet angle from LES, for different Re and W/d, in conjunction with the DDE model predictions, using the values of r, μ, k, and τ as optimized and indicated for each separate case. The thus obtained solutions of the model equation are in good agreement with the jet angle from the LES simulation, except for the inflexion points observed in the LES simulation that are not reproduced by the DDE model and which are probably due to higher order non-linear effects not taken into account in the model.

A. Reduced parameters

The non-linear delay model for a single jet in a confined cavity (Equation (10)) contains four constants, viz., r, μ, k, and τ. In terms of a dimensionless time $t' = rt$ and a scaled jet angle $\theta' = \sqrt{\mu/r}\theta$, the behavior of the model, however, is determined by only two independent parameters, $\alpha = k/r$ and $\delta = r\tau$,

$$\frac{d\theta'}{dt'} = \theta' - \theta'^3 - \alpha\theta'(t' - \delta). \tag{11}$$

Here, α denotes the relative strength of the feedback mechanism compared to the growth rate, and δ denotes the dimensionless delay time. Thus, as an alternative to r, μ, k, τ, model Equation (10) can also be defined in terms of $\alpha, \delta, \mu, \tau$. From a linear stability analysis of Equation (11), its neutral

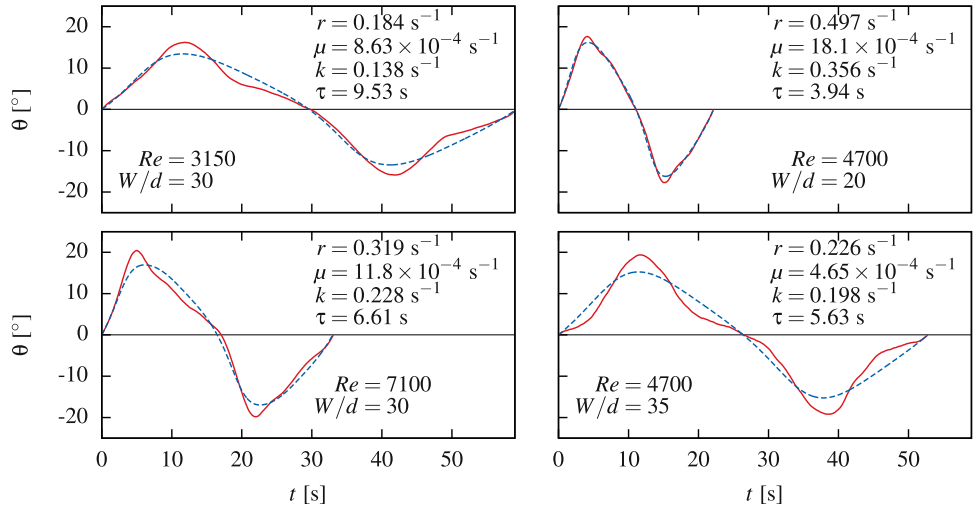

FIG. 9. Phase averaged jet angle profile from the LES simulations (solid red) and from the DDE model (dashed blue), for four cases with different Reynolds numbers and cavity widths. The model parameters r, μ, k, and τ obtained from the fitting procedure are shown per figure.

curve δ_n can be derived,[19]

$$\delta_n(\alpha) = \arccos\left(\frac{3\alpha - 2}{\alpha}\right)\left(\alpha^2 - (3\alpha - 2)^2\right)^{-\frac{1}{2}}. \tag{12}$$

For $\delta < \delta_n(\alpha)$, the oscillations vanish. The behavior of Equation (11) for $\alpha < 1$ is described by Suarez and Schopf.[19] They showed that the shape of the oscillation is sinusoidal close to the neutral curve $\delta = \delta_n(\alpha)$, while for $\delta \geq 10$, the oscillation reaches a block wave with a period of oscillation of twice the delay time.

The jet oscillations studied in this paper, see Figures 7 (right) and 8 (right), are of a sinusoidal nature, leading to the expectation that apparently the parameters α and δ in Equation (11) should be close to the neutral curve. This is indeed the case. Combinations of α and δ far above the critical curve were not observed for any studied combination of W/d and Re and seem to be unphysical for the studied flows.

Figure 10 shows the neutral curve, Equation (12), in conjunction with the found optimal values for α and δ for different sets of Re and W/d. Indeed, the best fit parameters all reside on, or very close to, the neutral curve. In other words, the number of parameters in the model can be reduced by one, to δ, μ, τ, by application of Equation (12) which relates δ to α. From Figure 10, it is also observed that α, i.e., the relative strength of the feedback compared to the initial growth rate, decreases for increasing Re, whereas α increases for increasing W/d.

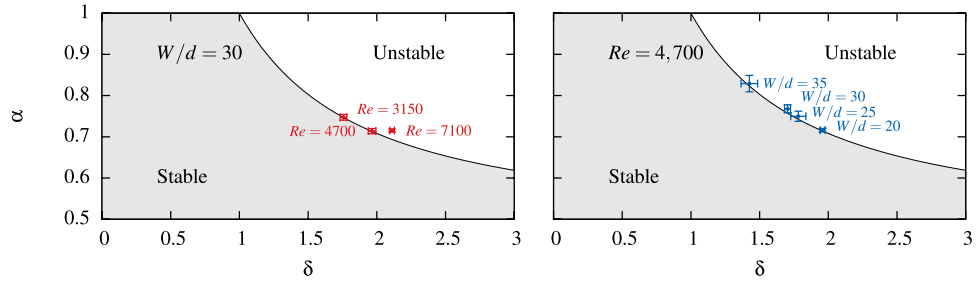

FIG. 10. The neutral curve (Equation (12)) of the reduced model (Equation (11)), where the shaded region depicts the region of stability, while the white region depicts the unstable modes. The parameter values for $Re = 3150$ up to $Re = 7100$ and $W/d = 30$ (left) and for $W/d = 20$ up to $W/d = 50$ and $Re = 4700$ (right) are depicted in this diagram. The error bars in these graphs indicate the accuracy in the fit, see the Appendix for details.

The parameter set can be further reduced by using a relation between μ and θ_{max}. Without the feedback term, it was derived that $\theta_{max} = \sqrt{r/\mu}$. By including the feedback term, however, the maximum jet angle should be slightly corrected, as for α and δ close to the neutral curve, it was found that $\theta'_{max} = \sqrt{2(1-\alpha^2)}$, and thus

$$\mu = \frac{2r\left(1-\alpha^2\right)}{\theta_{max}^2}. \tag{13}$$

Herewith, it is demonstrated that the parameter set $\{r, \mu, k, \tau\}$ can be reduced to $\{r, \tau\}$ by making use of relations (12) and (13) with $\alpha = k/r$ and $\delta = r\tau$.

B. Parameter estimation

From dimensional arguments, r and τ are expected to scale as

$$r = \kappa_1 \frac{v_{in}}{W} f\left(Re, \frac{W}{d}, \frac{H}{d}, \frac{d_n}{d}, \frac{T}{d}\right), \qquad \tau = \kappa_2 \frac{W}{v_{in}} g\left(Re, \frac{W}{d}, \frac{H}{d}, \frac{d_n}{d}, \frac{T}{d}\right). \tag{14}$$

From our LES simulations for varying Re ($1600 < Re < 7100$), W/d ($20 \le W/d < 50$), T/d ($3 \le T/d < 6$), H/d ($70 \le H/d \le 100$), and d_n/d ($10 \le d_n/d \le 25$), we find that $f = f(Re, W/d)$ and $g = g(Re, W/d)$, both being independent of T/d, H/d, and d_n/d for the studied range.

From a consecutive fitting procedure of the parameters, we determined r and τ as a function of v_{in}, W, Re, and W/d, as

$$r = \kappa_1 \frac{v_{in}}{W} Re^{-\frac{1}{4}} \left(\frac{W}{d}\right)^{-\frac{1}{2}}, \qquad \tau = \kappa_2 \frac{W}{v_{in}} Re^{\frac{5}{9}}, \tag{15}$$

with $\kappa_1 = 5.9 \pm 0.2$ and $\kappa_2 = 0.13 \pm 0.01$.

Figure 11 compares the results of the fit with the model estimation for the parameters r and τ (Equation (15)), showing a good agreement of our model with the parameters obtained from the LES simulations.

C. Model application

Validations of the presented model (Equation (10) with r, τ, μ, k obtained from Equations (12), (13), and (15)) are shown in Figure 12 for $Re = 4700$ and $W/d = 30$ and $Re = 7100$ and $W/d = 20$. The figure demonstrates the applicability of the present model for the prediction of the jet angle oscillation in a confined cavity for liquids of different viscosity and the independence of the model constants on T/d, H/d, and d_n/d for the studied ranges.

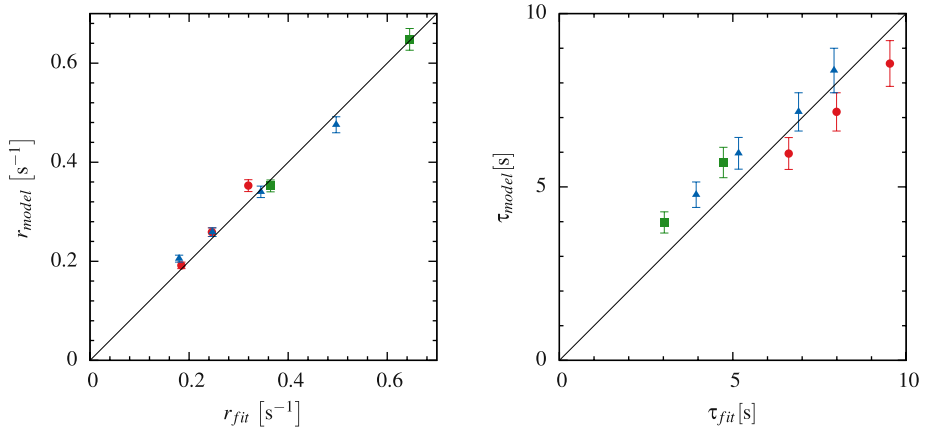

FIG. 11. Parity plot for r (left) and τ (right) following from the fit (horizontal axis) and the model (vertical axis, Equations (15)), for different Re (red circles for $W/d = 30$ and green squares for $W/d = 20$) and W/d (blue triangles for $Re = 4700$).

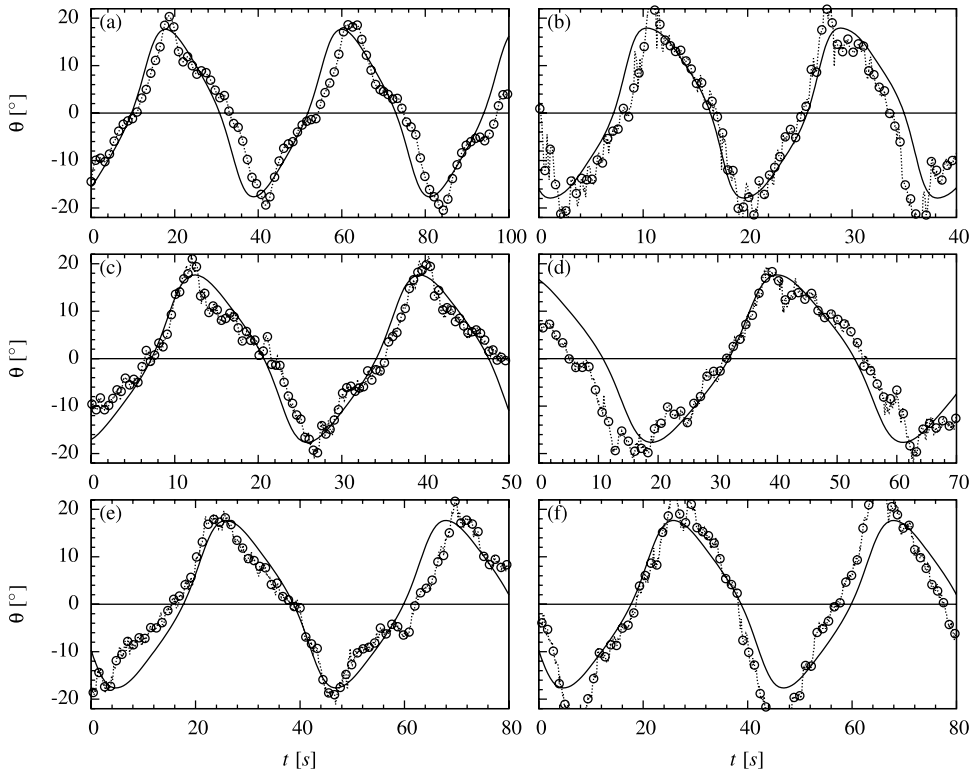

FIG. 12. Example model solutions (solid lines) and θ obtained from the numerical simulations (symbols and dashed lines). Unless stated otherwise, $T/d = 3.5$, $d_n/d = 10$, $H/d = 70$ (for $W/d < 50$) and $H/d = 2.5W/d$ (for $W/d \geq 50$) and $\nu = 1.0\times10^{-6}$ m^2/s, (a) $Re = 4700$ and $W/d = 30$, (b) $Re = 7100$ and $W/d = 20$, (c) $Re = 4700$, $W/d = 30$, $\nu = 2.0\times10^{-6}$ m^2/s and v_{in} changed accordingly to satisfy $Re = 4700$, (d) $Re = 4700$, $W/d = 30$, $T/d = 5.0$, (e) $Re = 4700$, $W/d = 30$, $H/d = 100$, (f) $Re = 4700$, $W/d = 30$, $d_n/d = 25$.

Of course, the frequency of an oscillating jet in a confined cavity for all Re and W/d may simply be calculated from the observed constant Strouhal number, $St = 0.011$. However, for sufficiently wide cavities, these oscillations are not present.[7,8] From Figure 10, it follows that the system is stable for $\delta < 1$. As $\delta = r\tau$, an approximate relation between the critical Reynolds number and the width to nozzle diameter ratio can be found,

$$Re_{crit} = \kappa_3 \left(\frac{W}{d}\right)^{\frac{18}{11}}, \tag{16}$$

with $\kappa_3 = (\kappa_1\kappa_2)^{-36/11} = 2.4 \pm 0.7$. This implies that

1. for certain W/d, there is a Re_{crit}, below which oscillations cease and
2. for certain Re, there is a $(W/d)_{crit}$, above which oscillations cease.

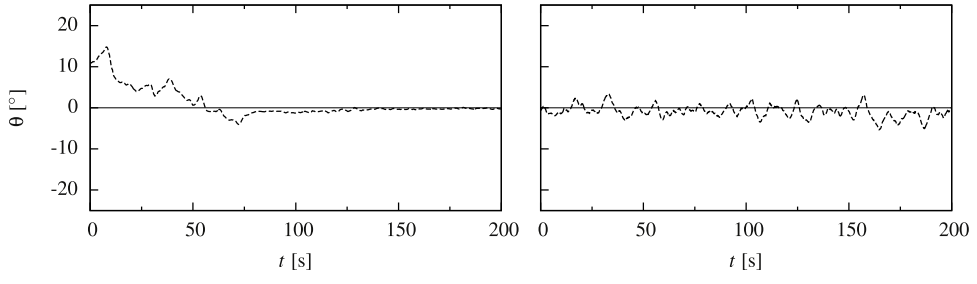

FIG. 13. The jet angle $\theta(t)$ for (left) $Re = 900$ and $W/d = 30$, initialized with the oscillating flow field for $Re = 1600$ and (right) $Re = 4700$ and $W/d = 100$, initialized with zero velocity in the domain.

TABLE I. For given Re and W/d, r and τ (Eq. (15)) are calculated. Furthermore, using Equation (16), Re_{crit} is calculated based on W/d. The last four columns indicate the oscillation frequency, based on $St = 0.011$, the LES model, the experiments by Kalter *et al.*,[6] and the zero-dimensional model, respectively. Unless stated otherwise, $H/d = 70$ (for $W/d < 50$) and $H/d = 2.5W/d$ (for $W/d \geq 50$), $d_n/d = 10$, $T/d = 3.5$ and $\nu = 1.27 \times 10^{-6}$ m^2/s.

Re	W/d	r (s^{-1})	τ (s)	Re_{crit}	f_{St} (Hz)	f_{LES} (Hz)	f_{exp} (Hz)	f_{model} (Hz)
500	30	0.05	19.2	~900	0.0023		No oscillations	$Re \leq Re_{crit}$
900	30	0.06	14.9	~900	0.0042	No oscillations		$Re \leq Re_{crit}$
1600	30	0.11	11.6	~900	0.0073	0.0098 ± 0.004		0.0095
1600	50	0.09	11.8	~2000	0.0044	No oscillations		$Re \leq Re_{crit}$
3150	20	0.35	5.71	~400	0.022	0.034 ± 0.003		0.032
3150	30	0.19	8.56	~900	0.015	0.017 ± 0.001	0.014	0.018
4700	20	0.48	4.75	~400	0.033	0.045 ± 0.002		0.042
4700	25	0.34	5.94	~600	0.026	0.032 ± 0.002		0.031
4700	30	0.26	7.11	~900	0.022	0.022 ± 0.001	0.022	0.024
4700	35	0.21	8.32	~1100	0.019	0.015 ± 0.002		0.019
4700	50	0.12	11.9	~2000	0.013	0.006 ± 0.002		0.011
4700	100	0.04	23.8	~6000	0.0066	No oscillations		$Re \leq Re_{crit}$
7100	20	0.65	3.98	~400	0.050	0.059 ± 0.005		0.054
7100	30	0.35	5.98	~900	0.033	0.031 ± 0.002	0.035	0.031
10 000	30	0.46	5.12	~900	0.047		0.042	0.039
4700	30	0.41	4.55	~900	0.034	0.035 ± 0.002		0.037[a]
4700	30	0.26	7.11	~900	0.022	0.020 ± 0.003		0.024[b]
4700	30	0.26	7.11	~900	0.022	0.021 ± 0.003		0.024[c]
4700	30	0.26	7.11	~900	0.022	0.024 ± 0.004		0.024[d]

[a] $\nu = 2.0 \times 10^{-6}$ m^2/s.
[b] $T/d = 5.0$.
[c] $H/d = 100$.
[d] $d_n/d = 25$.

The ceasing of the oscillations is demonstrated in Figure 13, which shows the jet angle for $Re = 900$ and $W/d = 30$ and for $Re = 4700$ and $W/d = 100$. According to the above Re_{crit}, the oscillations of the jet angle should vanish for these conditions, and indeed, no periodic jet oscillations are observed.

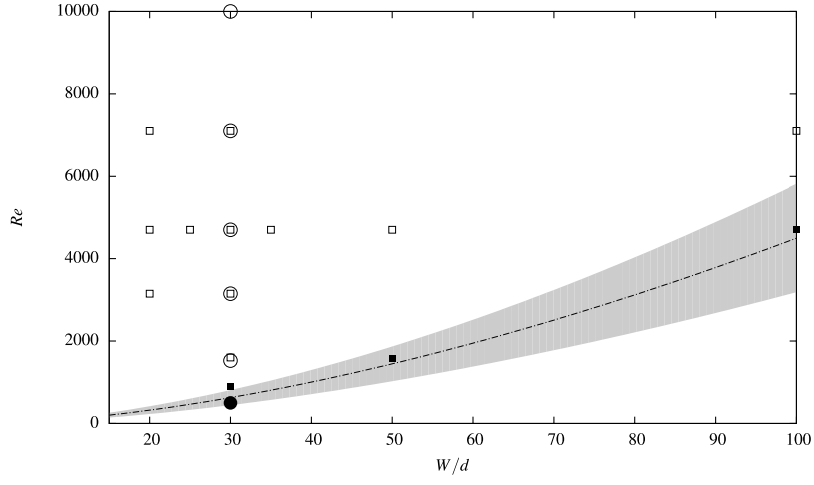

FIG. 14. Flow stability as a function of Re and W/d for simulations (squares) and experiments (circles). Oscillatory flows are indicated by open symbols, non-oscillating flow by closed symbols. The critical Reynolds number predicted by the DDE model, with its uncertainty, is depicted by the solid line and grey area, respectively. Oscillatory flows are expected for $Re > Re_{crit}$. For all symbols $T/d = 3.5$, $d_n/d = 10$, and $\nu = 1.27 \times 10^{-6}$ m^2/s.

In Table I, we summarize, for the cases in Figures 12 and 13, r, τ, Re_{crit}, $(W/d)_{crit}$ as well as frequencies following from $St = 0.011$, the LES simulation, the experiments by Kalter *et al.*, and the DDE model. From this table, it also follows why the oscillations vanish. The growth rate of the supposed jet angle oscillation becomes very weak, such that a possible deflection of the jet does not get amplified significantly.

The stable and oscillating modes listed in Table I are summarized in a flow stability diagram in Figure 14 in conjunction with the critical curve (Equation (16)).

VI. CONCLUSION

We studied the dynamics of the self-sustained oscillation of a turbulent jet in a confined cavity. We presented a zero-dimensional DDE-type model that describes the oscillation of the jet angle in such a system. The model includes the three consecutive phases of the jet oscillation, which are the pressure driven growth of the oscillation, the limited amplitude due to the confinement, and the delayed destruction of the pressure deficit in the recirculation zone by a feedback loop. These phases are described by their respective terms in a delay differential equation with four parameters. We showed that the dimensionless behavior of the model can be properly represented by just two parameters, which are the growth rate of the oscillation, r, and the delay time, τ, for the destruction of the strong recirculation zone adjacent to the oscillating jet. Closed relations have been proposed for both parameters as a function of the jet Reynolds number Re, the inlet velocity v_{in}, the cavity width W, and the cavity width to nozzle diameter ratio W/d. For the studied ranges ($3 < T/d < 6$, $70 < H/d < 100$, $10 < d_n/d < 25$) both model parameters are independent of these geometry ratios.

The model displays the correct oscillation behavior of the jet across the domain for ranges of at least $1600 < Re < 7100$ and $20 \leq W/d < 50$ when these are compared with three dimensional large eddy simulations. The model also describes that jet oscillations vanish for Reynolds numbers below a critical value, and W/d above a critical value, which both can be predicted *a priori*. As this model includes the prediction of stable modes, it can be of interest for all kinds of industrial applications where the stabilization of oscillating flows is relevant. This model also offers perspective for pressure dominated oscillations in multi-jet configurations and more irregular oscillations, by additionally introducing two oscillators and multiple delay terms, respectively.

ACKNOWLEDGMENTS

This work was supported by the Dutch Technology Foundation STW, Tata Steel, and ABB. We thank SURFsara for the support in using the Lisa Compute Cluster, Project Code No. MP-235-12. We thank Jasper Hollander for his assistance in the initial set-up of the numerical simulations.

APPENDIX: *A POSTERIORI* DETERMINATION OF THE MODEL PARAMETERS

The proposed model (Equation (10)) for the jet oscillation comprises four unknowns, the growth factor r, the obstruction factor μ, the delay time τ and the delay strength k. These parameters can be obtained from fitting the solution of Equation (10) with a realization of the jet angle as a function of time. The fitting procedure for obtaining r, μ, k, and τ is as follows and is calculated using MATLAB-R2013b.

1. Calculation of the phase average of $\theta(t)$.
2. Loop over different sets $\{r, \mu, k, \tau\}$ of initial conditions.
   (a) Calculate phase of periodic solution by solving Equation (10) for one or more sets of $\{r, \mu, k, \tau\}$ using Matlab's `dde23` routine.[35] This routine is able to solve (systems of) non-linear differential delay equations of the form $y'(t) = f(t, y(t), y(t-\tau))$.
   (b) Calculate the value of the cost function (Equation (A1)) for the solution.
   (c) Apply the Nelder-Mead simplex method[34] on the parameters and repeat from step (a) until convergence is reached.

The determination of the parameters includes a loop over several sets of initial conditions, since the minimum found by the Nelder-Mead method is not necessarily a global minimum. From 10 different initial values, we select the solution with the lowest value of the cost function.

1. Phase average

The phase average $\tilde{\theta}(t)$ is calculated from the time signal $\theta(t)$ by rescaling each period, defined from positive zero-crossing to the next positive zero-crossing, to the dominant period, and subsequent averaging of the phases, finally the phase average is rescaled to the mean peak value. Thus,

1. Determine t_i, the ith zero-crossing (where $\theta(t = t_i) = 0$).
2. Define the ith phase, $\theta_i(t)$ from $\theta(t)$ between $t_{i-1} < t < t_i$.
3. Define the stretched phase $\theta_i^*(t') = \theta_i\left(\frac{t-t_{i-1}}{\mathcal{T}_i}\right)$ with $\mathcal{T}_i = t_i - t_{i-1}$.
4. Calculate the phase average $\widetilde{\theta^*}(t') = \frac{1}{N}\sum_{i=1}^{N}\theta_i^*(t^*)$ and the mean amplitude $\overline{\theta^*} = \frac{1}{N}\sum_{i=1}^{N}\max\theta_i^*$.
5. Rescale the phase average $\widetilde{\theta}(t) = \widetilde{\theta^*}(t/\mathcal{T})\dfrac{\overline{\theta^*}}{\max\widetilde{\theta^*}}$.

2. Cost function

The cost function that is minimized in the Nelder-Mead method is defined as

$$f(\theta,\tilde{\theta}) = m_1 m_2 m_3 \frac{\int_0^{\mathcal{T}_{\tilde{\theta}}}(\tilde{\theta}-\theta)^2 dt}{\int_0^{\mathcal{T}_{\tilde{\theta}}}\tilde{\theta}^2 dt}, \tag{A1}$$

which is the normalized root-mean-square distance between the phase-averaged $\tilde{\theta}$ and the calculated θ, multiplied by additional multipliers, m_1, m_2, and m_3 in order to improve the convergence rate of the algorithm, i.e.,

- if the oscillation period $\mathcal{T}_\theta$ is different from the intended period: $\mathcal{T}_{\tilde{\theta}}$. $m_1 = 1 + 10(\max\left(\frac{\mathcal{T}_\theta}{\mathcal{T}_{\tilde{\theta}}}, \frac{\mathcal{T}_{\tilde{\theta}}}{\mathcal{T}_\theta}\right) - 1)$,
- if any of r, μ, k, $\delta - 1$ or $\delta - \delta_n(\alpha)$ is negative: $m_2 = \prod_{q\in\{r,k,\mu,\delta,\delta-\delta_n(\alpha)\}} 1 - 100\min(0,q)$,
- if $\alpha > 1$: $m_3 = 1 + 100(\max(\alpha,1) - 1)$.

3. Error estimation

In order to quantify the error in our fitting procedure, we use a bootstrapping of resampling residuals. If we denote the original phase-averaged signal by θ_i and the fit by θ_i^*, then the residual is defined as $\varepsilon_i = \theta_i - \theta_i^*$. Now, the fitting procedure is repeatedly executed on $\hat{\theta}_i = \theta_i^* + \varepsilon_j$. The error in r, μ, k, and τ is obtained as the standard deviation of the resulting sets of parameter values. The error in α and δ is then straightforwardly obtained.

[1] G. Bouchet and E. Climent, "Unsteady behavior of a confined jet in a cavity at moderate Reynolds numbers," Fluid Dyn. Res. **44**, 025505 (2012).
[2] E. Villermaux and E. Hopfinger, "Self-sustained oscillations of a confined jet: A case study for the non-linear delayed saturation model," Phys. D **72**, 230–243 (1994).
[3] A. Maurel, P. Ern, B. J. A. Zielinska, and J. E. Wesfreid, "Experimental study of self-sustained oscillations in a confined jet," Phys. Rev. E **54**, 3643–3651 (1996).
[4] T. Kolšek, N. Jelić, and J. Duhovnik, "Numerical study of flow asymmetry and self-sustained jet oscillations in geometrically symmetric cavities," Appl. Math. Modell. **31**, 2355–2373 (2007).
[5] N. A. Molloy and P. L. Taylor, "Oscillatory flow of a jet into a blind cavity," Nature **224**, 1192–1194 (1969).
[6] R. Kalter, M. J. Tummers, S. Kenjereš, B. W. Righolt, and C. R. Kleijn, "Effects of electromagnetic forcing on self-sustained jet oscillations," Phys. Fluids **26**, 065101 (2014).
[7] A. Mataoui and R. Schiestel, "Unsteady phenomena of an oscillating turbulent jet flow inside a cavity: Effect of aspect ratio," J. Fluids Struct. **25**, 60–79 (2009).
[8] J. R. Landel, C. P. Caulfield, and A. W. Woods, "Meandering due to large eddies and the statistically self-similar dynamics of quasi-two-dimensional jets," J. Fluid Mech. **692**, 347–368 (2012).

[9] N. Lawson and M. Davidson, "Self-sustained oscillation of a submerged jet in a thin rectangular cavity," J. Fluids Struct. **15**, 59–81 (2001).
[10] R. M. Fearn, T. Mullin, and K. A. Cliffe, "Nonlinear flow phenomena in a symmetric sudden expansion," J. Fluid Mech. **211**, 595–608 (1990).
[11] D. Drikakis, "Bifurcation phenomena in incompressible sudden expansion flows," Phys. Fluids **9**, 76–87 (1997).
[12] M. P. Escudier, P. J. Oliveira, and R. J. Poole, "Turbulent flow through a plane sudden expansion of modest aspect ratio," Phys. Fluids **14**, 3641–3654 (2002).
[13] D. Rockwell and E. Naudascher, "Self-sustained oscillations of impinging free shear layers," Annu. Rev. Fluid Mech. **11**, 67–94 (1979).
[14] T. Shakouchi, "New fluidic oscillator, flowmeter, without control port and feedback loop," J. Dyn. Sys., Meas., Control **111**, 535–539 (1989).
[15] C. W. Rowley, T. Colonius, and A. J. Basu, "On self-sustained oscillations in two-dimensional compressible flow over rectangular cavities," J. Fluid Mech. **455**, 315–346 (2002).
[16] A. Powell, "On the edgetone," J. Acoust. Soc. Am. **33**, 395–409 (1961).
[17] M. C. Mackey and L. Glass, "Oscillation and chaos in physiological control systems," Science **197**, 287–289 (1977).
[18] M. Szydlowski, A. Krawiec, and J. Tobola, "Nonlinear oscillations in business cycle model with time lags," Chaos, Solitons Fractals **12**, 505–517 (2001).
[19] M. Suarez and P. Schopf, "A delayed action oscillator for ENSO," J. Atmos. Sci. **45**, 3283–3287 (1988).
[20] I. Boutle, R. H. S. Taylor, and R. A. Römer, "El Niño and the delayed action oscillator," Am. J. Phys. **75**, 15–24 (2007).
[21] E. Villermaux, "Memory-induced low frequency oscillations in closed convection boxes," Phys. Rev. Lett. **75**, 4618–4621 (1995).
[22] H. G. Weller, G. Tabor, H. Jasak, and C. Fureby, "A tensorial approach to computational continuum mechanics using object-oriented techniques," Comput. Phys. **12**, 620–631 (1998).
[23] R. I. Issa, "Solution of the implicitly discretised fluid flow equations by operator-splitting," J. Comput. Phys. **62**, 40–65 (1986).
[24] D. K. Lilly, "A proposed modification of the Germano subgrid-scale closure method," Phys. Fluids A **4**, 633 (1992).
[25] Y. Zang, R. L. Street, and J. R. Koseff, "A dynamic mixed subgrid-scale model and its application to turbulent recirculating flows," Phys. Fluids A **5**, 3186–3196 (1993).
[26] V. Vuorinen, J. P. Keskinen, C. Duwig, and B. J. Boersma, "On the implementation of low-dissipative Runge-Kutta projection methods for time dependent flows using OpenFOAM," Comput. Fluids **93**, 153–163 (2014).
[27] D. B. Spalding, "A single formula for the law of the wall," J. Appl. Mech. **28**, 455–458 (1961).
[28] E. de Villiers, "The potential of large eddy simulation for the modeling of wall bounded flows," Ph.D. thesis, Imperial College, London, 2006.
[29] C. Duprat, G. Balarac, O. Métais, P. M. Congedo, and O. Brugière, "A wall-layer model for large-eddy simulations of turbulent flows with/out pressure gradient," Phys. Fluids **23**, 015101 (2011).
[30] A. Martín-Alcántara, E. Sanmiguel-Rojas, C. Gutiérrez-Montes, and C. Martínez-Bazán, "Drag reduction induced by the addition of a multi-cavity at the base of a bluff body," J. Fluids Struct. **48**, 347–361 (2014).
[31] W. P. Jones, "Turbulence modelling and numerical solution methods for variable density and combusting," in *Turbulent Reacting Flows* (Academic Press Inc., 1994), pp. 309–374.
[32] See supplementary material at http://dx.doi.org/10.1063/1.4930926 for the geometrical derivation of the maximum jet angle.
[33] M. Lakshmanan and D. V. Senthilkumar, *Dynamics of Nonlinear Time-Delay Systems* (Springer, Berlin, Heidelberg, 2010).
[34] J. A. Nelder and R. Mead, "A simplex method for function minimization," Comput. J. **7**, 308–313 (1965).
[35] L. F. Shampine and S. Thompson, "Solving DDEs in MATLAB," Appl. Numer. Math. **37**, 441–458 (2001).